



Original Article

Development and validation of multiphysics PWR core simulator KANT



Taesuk Oh, Yunseok Jeong, Husam Khalefah, Yonghee Kim*

Department of Nuclear & Quantum Engineering, Korea Advanced Institute of Science and Technology, 291 Daehak-ro Yuseong-gu, Daejeon, 34141, South Korea

ARTICLE INFO

Article history:

Received 4 August 2022

Received in revised form

20 January 2023

Accepted 16 February 2023

Available online 18 February 2023

Keywords:

PWR core Simulator

Multi-group nodal method

Thermal-hydraulics feedback

Multi-physics

Macroscopic depletion

Validation

ABSTRACT

KANT (KAIST Advanced Nuclear Tachygraphy) is a PWR core simulator recently developed at Korea Advance Institute of Science and Technology, which solves three-dimensional steady-state and transient multigroup neutron diffusion equations under Cartesian geometries alongside the incorporation of thermal-hydraulics feedback effect for multi-physics calculation. It utilizes the standard Nodal Expansion Method (NEM) accelerated with various Coarse Mesh Finite Difference (CMFD) methods for neutronics calculation. For thermal-hydraulics (TH) calculation, a single-phase flow model and a one-dimensional cylindrical fuel rod heat conduction model are employed. The time-dependent neutronics and TH calculations are numerically solved through an implicit Euler scheme, where a detailed coupling strategy is presented in this paper alongside a description of nodal equivalence, macroscopic depletion, and pin power reconstruction. For validation of the steady, transient, and depletion calculation with pin power reconstruction capacity of KANT, solutions for various benchmark problems are presented. The IAEA 3-D PWR and 4-group KOEBERG problems were considered for the steady-state reactor benchmark problem. For transient calculations, LMW (Lagenbuch, Maurer and Werner) LWR and NEACRP 3-D PWR benchmarks were solved, where the latter problem includes thermal-hydraulics feedback. For macroscopic depletion with pin power reconstruction, a small PWR problem modified with KAIST benchmark model was solved. For validation of the multi-physics analysis capability of KANT concerning large-sized PWRs, the BEAVRS Cycle1 benchmark has been considered. It was found that KANT solutions are accurate and consistent compared to other published works.

© 2023 Korean Nuclear Society. Published by Elsevier Korea LLC. This is an open access article under the CC BY-NC-ND license (<http://creativecommons.org/licenses/by-nc-nd/4.0/>).

1. Introduction

For designing the pressurized water reactor (PWR) and performing safety analysis, assessment of the steady-state multiplication factor, burnup dependent attributes, and dynamic behaviour of the reactor system is imperative. Considering both accuracy and computing efficiency, the conventional ‘two-step’ system such as CASMO/SIMULATE, DeCART/MASTER, SCALE/PARCS, and Serpent2/ARES still serves as the cornerstone for modern reactor analysis, where transport and diffusion calculations are applied for assembly-wise and whole core problems respectively [1–7]. Note that the assembly-wise transport calculation result, which is often referred to as lattice calculation, must be condensed (or) homogenized into assembly-wise few-group cross-sections, and the

whole core configuration is represented based on such homogenized quantities.

Intuitively, the two-step procedure implies that the accuracy of the final outcome from the whole core calculation hinges upon the extent of preservation of high-fidelity information, i.e., transport-based lattice calculation. For such a purpose, various homogenization processes including the generalized equivalence theory (GET) have been proposed and commonly employed in modern reactor analyses [8]. Nevertheless, it is still imperative to have a reliable whole core solution within a moderate computing burden from the diffusion calculation. Whereupon, nodal methods coupled with a coarse-mesh finite difference (CMFD) like acceleration scheme are widely accepted.

In addition, the presence of a strong feedback phenomenon originating from the thermal-hydraulics (TH) effect must be included in the calculation for a realistic appraisal. Such interdependency between the neutronics and TH calculations should be aptly considered whilst generating the homogenized cross-

* Corresponding author.

E-mail address: yonghekim@kaist.ac.kr (Y. Kim).

sections, and proper thermal balance equations must be solved for steady-state, macroscopic depletion, and transient whole core diffusion calculations to incorporate the TH feedback effect.

Since the conventional two-step approach is based on assembly-wise homogenization, for acquiring the pin-wise localized information, assumption(s) is inevitably introduced. To circumvent such an inherent drawback, a pin-wise two-step calculation could be performed. However, the pin-wise whole core diffusion calculation may incur a considerable computing burden unless a special measure like that of the Hybrid-CMFD (HCMFD) is taken [9]. Therefore, the reconstruction process is often implemented for estimating the pin-wise quantities [10].

Recently, KAIST Advanced Nuclear Tachygraphy (KANT) has been developed at KAIST which is a multi-physics three-dimensional space-time PWR simulator sufficing the aforementioned considerations. For steady-state and transient neutronics calculation, KANT solves the neutron diffusion equation in Cartesian geometries based on the Nodal Expansion Method [11,12] accelerated through the CMFD acceleration scheme. For procuring the nodal equivalence, discontinuity factors are considered for every surface of a node of computation, including the axial direction. To accommodate the thermal-hydraulics feedback effect, KANT is equipped with a simplified thermal-hydraulics module that consists of a cylindrical heat conduction model for the fuel pin, and a one-dimensional single-phase flow model under constant pressure for the coolant. The change in the thermal-hydraulics quantities is reflected in the neutronics calculation through proper derivative terms in the homogenized few-group cross-sections [3]. For depletion analysis, a so-called predictor-corrector scheme-based macroscopic depletion is performed, where special treatment is drawn upon xenon and samarium decay chains [13].

To verify the accuracy of KANT solutions, various benchmarks are solved and their results are presented in this paper. The contents of the paper are organized as follows: In Section 2, a detailed description of the theories for the multi-physics calculation of KANT is presented. It includes not only the models for neutronics and TH calculations, but incorporates remarks on the rod cusping issue, nodal equivalence, macroscopic depletion, and pin power reconstruction. In Section 3, a description of various benchmarks with KANT calculation results is shown. Finally, conclusions alongside future improvements of KANT are discussed in Section 4.

2. Theory and model

2.1. Multi-group neutron diffusion equation

To calculate the multiplication factor of a reactor system, the steady-state multi-group diffusion equation is solved.

$$M_g \phi_g = \frac{\chi_g}{k_{\text{eff}}} \sum_{g'=1}^G \nu \Sigma_{f,g'} \phi_{g'} + \sum_{g'=1}^G \Sigma_{s,g' \rightarrow g} \phi_{g'}, \quad (1)$$

(g' ≠ g)

where G and k_{eff} represents the number of energy groups and multiplication factor, M_g denotes the migration operator for group g ($M_g \phi_g := -\nabla \bullet D_g \nabla \phi_g + \Sigma_{r,g} \phi_g$), and all the other notations are that of the convention.

The transient multi-group diffusion equation is expressed through the following two sets of system of equations, including the balance for precursor concentration.

$$\begin{aligned} \frac{1}{\nu_g} \frac{\partial \phi_g}{\partial t} &= -M_g \phi_g(\mathbf{r}, t) + \sum_{g'=1}^G \Sigma_{s,g' \rightarrow g} \phi_{g'} + (1 - \beta) \frac{\chi_g}{k_{\text{eff}}} F\phi(\mathbf{r}, t) \\ &\quad + \sum_{k=1}^{G_d} \lambda_k \chi_{g,k} C_k(\mathbf{r}, t), \end{aligned} \quad (2)$$

$$\frac{\partial C_k}{\partial t} = -\lambda_k C_k(\mathbf{r}, t) + \frac{\beta_k}{k_{\text{eff}}} F\phi(\mathbf{r}, t), \quad (3)$$

where subscript k represents precursor group indexes, and $F\phi(\mathbf{r}, t)$ is defined as below:

$$F\phi(\mathbf{r}, t) := \sum_{g=1}^G \nu \Sigma_{f,g} \phi_g(\mathbf{r}, t). \quad (4)$$

Notations $\beta = \sum_{k=1}^{G_d} \beta_k$, and $\chi_{g,k}$ represents the contribution of precursor-born neutrons from the precursor C_k that contributes to group g , where the number of delayed neutron groups is denoted with G_d .

Implementation of implicit-Euler scheme, exponential transformation of the flux, and linear variation of $F\phi(\mathbf{r}, t)$ term renders the above equations as below [14]:

$$\begin{aligned} \left(\frac{1}{\nu_g \Delta t_s} + \frac{\gamma_s}{\nu_g} + M_g \right) \phi_g^{(l+1)}(t_s) &= (1 - \beta) \frac{\chi_g}{k_{\text{eff}}} F\phi^{(l)}(t_s) + S\phi^{(l)}(t_s) \\ &\quad + \sum_{k=1}^6 \lambda_k \chi_{g,k} C_k(t_{s-1}) f_{1,k} + \sum_{k=1}^6 \frac{\chi_{g,k} \beta_k F\phi(t_{s-1})}{k_{\text{eff}}} f_{2,k} \\ &\quad + \sum_{k=1}^6 \frac{\chi_{g,k} \beta_k F\phi^{(l)}(t_s)}{k_{\text{eff}}} f_{3,k} + \frac{e^{\gamma_s \Delta t_s}}{\nu_g \Delta t_s} \phi_g(t_{s-1}), \end{aligned} \quad (5)$$

$$C_k(t_s) = C_k(t_{s-1}) f_{1,k} + \frac{\beta_k F\phi(t_{s-1})}{\lambda_k k_{\text{eff}}} f_{2,k} + \frac{\beta_k F\phi(t_s)}{\lambda_k k_{\text{eff}}} f_{3,k}, \quad (6)$$

where upper-script l is the iteration index. Notations $f_{1,k}$, $f_{2,k}$, $f_{3,k}$, and $S\phi(t_s)$ are expressed as:

$$f_{1,k} = e^{-\lambda_k \Delta t_s}$$

$$\begin{aligned} f_{2,k} &= \frac{1 - e^{-\lambda_k \Delta t_s} - \lambda_k \Delta t_s e^{-\lambda_k \Delta t_s}}{\lambda_k \Delta t_s} \\ f_{3,k} &= \frac{e^{-\lambda_k \Delta t_s} (1 - e^{\lambda_k \Delta t_s} + \lambda_k \Delta t_s e^{\lambda_k \Delta t_s})}{\lambda_k \Delta t_s}, \end{aligned} \quad (7)$$

$$\begin{aligned} S\phi(t_s) &= \sum_{g'=1}^G \Sigma_{s,g' \rightarrow g} \phi_{g'}(t_s). \\ &\quad (g' \neq g) \end{aligned} \quad (8)$$

with the transformation constant γ_s being determined as

$$\gamma_s = \frac{1}{\Delta t_s} \ln \left(\frac{\phi(t_{s-1})}{\phi(t_{s-2})} \right). \quad (9)$$

The discretization scheme, e.g., nodal expression, determines the group-wise migration operator M_g in a matrix form.

2.2. Nodal expansion method

As aforementioned, KANT employs the standard Nodal Expansion Method (NEM) to discretize the neutron balance equation, which is accelerated through various coarse-mesh finite difference (CMFD) schemes [15]. Through integration of Eq. (1) over y - and z -directions without losing generality, a one-dimensional balance equation is obtained.

$$\begin{aligned} -\frac{D_g^i}{(h_x^i)^2} \frac{\partial^2}{\partial \xi_x^2} \phi_{g,x}^i(\xi_x) + \Sigma_{r,g}^i \phi_{g,x}^i(\xi_x) &= \sum_{g'=1}^G \Sigma_{s,g' \rightarrow g}^i \phi_{g',x}^i(\xi_x) \\ &\quad (g'=g) \\ &+ \frac{\chi_g}{k} \sum_{g'=1}^G \nu \Sigma_{f,g}^i \phi_{g',x}^i(\xi_x) - L_{gx}^i(\xi_x), \end{aligned} \quad (10)$$

where i denotes the node of interest with a size of $h_x^i \times h_y^i \times h_z^i$, $\xi_x (= x/h_x^i)$ represents the normalized coordinate ranging from -0.5 to $+0.5$, and $L_{gx}^i(\xi_x)$ is the transverse leakage. The flux and transverse leakage terms for a certain direction are expanded through 4-th and 2-nd order polynomial basis functions respectively in NEM. Further detailed explanation can be found elsewhere [3].

The underlying philosophy of CMFD-based acceleration is to retain the higher-order solution-based current information whilst utilizing the simple finite difference method (FDM) through the usage of correction factor(s). Determination of the net current corresponds to the calculation of flux expansion coefficients, in which $4G$ (G = number of groups) number of coefficients are required for NEM whilst solving a certain node of interest. For a two-node configuration, a total of $8G$ coefficients needs to be calculated to determine the current at the interface which demands the same number of governing equations: flux continuity (1G), current continuity (1G), 0-th, 1-st, and 2-nd moment balance equation (2G for each). For a single-node configuration, which corresponds to the peripheral node facing a certain boundary condition, incoming partial current information (or albedo) is employed in lieu of continuity equations to determine a total of $4G$ coefficients [3].

2.3. Nodal equivalence

Since the accuracy of the two-step procedure strongly depends on the extent of conveying the high-fidelity transport-based lattice calculation result to the whole core diffusion analysis, a measure for retaining accurate current information is required. The reactor balance equation, which could be interpreted as an eigenvalue problem, is a well-defined problem. Hence, when the net current information across the nodes is preserved, one could attain the reference eigenvalue of the problem. For such a purpose, a concept of discontinuity factor (DF) have been devised, which is a cornerstone for the generalized equivalence theory (GET) [8]:

$$DF_{gsi} := \frac{\phi_{gsi}^{het}}{\phi_{gsi}^{hom}}, \quad (11)$$

where ϕ_{gsi}^{hom} and ϕ_{gsi}^{het} denote homogeneous and heterogeneous

(reference) surface flux for group g at the surface s of mesh of interest i . Note that ϕ_{gsi}^{hom} is determined based on the homogenized cross-sections with a specific diffusion-based method, hence the DF is inherently methodology dependent unless the lattice calculation is performed under whole reflective boundary condition. For the latter case, the homogeneous flux becomes flat due to the neglection of the diffusion term, and the acquired DF is referred to as the assembly discontinuity factor (ADF).

The acquired DF value is then subsumed in the nodal-based flux continuity equation, where intentional discontinuity in the surface flux is introduced between the contiguous nodes. Such a treatment preserves the reference surface flux and the current, which leads to a retainment of the high-fidelity calculation result. The KANT neutronics calculation not only takes into account the radial direction DF but also the axial-wise DF values.

2.4. Thermal-hydraulics model

To model the feedback phenomenon from the thermal-hydraulics effect, both the balance equations for the flow of the moderator and heat transfer across the fuel pin should be considered. The spatial temperature and pressure distribution of the moderator can be calculated from mass continuity equation, momentum balance equation, and energy balance (or heat) equation. For simplicity, both cross-flow and pressure drop are neglected in the simulation, which rules out the need for solving the momentum balance equation. Fig. 1 depicts a certain control volume i in an axial direction where $q''_F(t)$ denotes the heat flux from the fuel rod, $q''_M(t)$ represents the heat density from fission that directly dissipates in the coolant, and all the other notations are that of the convention.

Mass continuity equation.

$$A_{flow} \frac{\partial \rho}{\partial t} + \frac{\partial \dot{m}}{\partial z} = 0. \quad (12)$$

Heat equation

$$A_{flow} \frac{\partial(\rho h)}{\partial t} + \frac{\partial(\dot{m}h)}{\partial z} = P_H q''_F(t) + A_{flow} q''_M(t). \quad (13)$$

Implementation of implicit-Euler and upwind scheme, Eqs. (12) and (13) can be discretized as below:

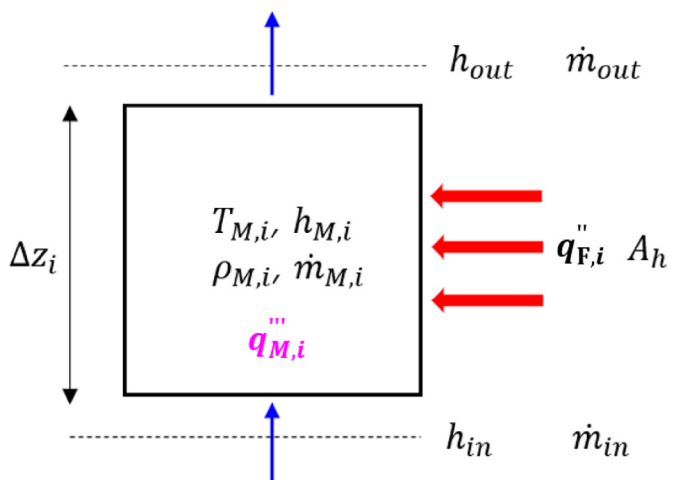


Fig. 1. Representative cartoon for thermal-hydraulics balance equation for coolant.

$$\dot{m}_{M,i}^{(l+1)}(t_s) = \dot{m}_{M,i-1}(t_s) - \Delta z_i A_{flow} \left[\frac{\rho_{M,i}^{(l)}(t_s) - \rho_{M,i}(t_{s-1})}{\Delta t_s} \right], \quad (14)$$

$$Q_{i-1,i} = K_{i-1,i}(\bar{T}_{i-1} - \bar{T}_i), \quad (19)$$

$$K_{i-1,i} = \frac{2\pi r_{i-1} k_i k_{i-1}}{k_i(r_{i-1} - \bar{r}_{i-1}) + k_{i-1}(\bar{r}_i - r_{i-1})} \bullet dz, \quad (20)$$

$$h_{M,i}^{(l+1)}(t_s) = \frac{q''_{F,i}(t_s)A_h + q'''_{M,i}(t_s)\Delta z_i A_{flow} + \dot{m}_{M,i-1}(t_s) h_{M,i-1}(t_s) + \Delta z_i A_{flow} \bullet \frac{\rho_{M,i}(t_{s-1})h_{M,i}(t_{s-1})}{\Delta t_s}}{\dot{m}_{M,i}^{(l+1)}(t_s) + \Delta z_i A_{flow} \bullet \frac{\rho_{M,i}^{(l)}(t_s)}{\Delta t_s}}, \quad (15)$$

where upper-script l is the iteration index. It is worthwhile to articulate that the updated egressing quantities from Eqs. (14) and (15) ingress to the contiguous node, where series of calculation determines the axial temperature distribution within the reactor core.

The acquired moderator temperature distribution then serves as a boundary condition for ascertaining the temperature distribution within the fuel rods. The governing balance equation for a control volume within a fuel rod can be expressed as

$$\rho c_p \frac{\partial T}{\partial t} + \nabla \bullet \bar{q}'' = q''', \quad (16)$$

where ρ , c_p , \bar{q}'' , and q''' indicate density [kg/m^3], heat capacity [$\text{J}/\text{kg}\cdot\text{K}$], heat flux [W/m^2], and heat density [W/m^3] respectively. KANT uses finite-volume method (FVM) for discretizing Eq. (16), where the overall configuration is depicted in Fig. 2 [16,17]. The temperature within the fuel region is calculated at the radial position \bar{r}_i defined as

$$\bar{r}_i = \frac{1}{\pi(r_i^2 - r_{i-1}^2)} \int_{r_{i-1}}^{r_i} dr 2\pi r^2 = \frac{2}{3} \frac{r_i^2 + r_i r_{i-1} + r_{i-1}^2}{r_i + r_{i-1}}, \quad (17)$$

where r_i denotes the equally spaced points spanning the fuel rod in a radial direction. For the pellet-to-clad gap region, the computational point resides on the outer surface of the pellet (\bar{r}_{N-2}), and for clad regions, temperature points are computed at clad inner and outer faces (\bar{r}_{N-1} and \bar{r}_N).

Integration of Eq. (16) for each node yields the following equation:

$$(\rho c_p V)_i \frac{\partial \bar{T}_i}{\partial t} = Q_{i-1,i} + Q_{i+1,i} + q''_i V_i, \quad (18)$$

where V_i denotes the node volume [m^3], and Q_{ij} represents the heat flow [W] from node i to node j . For the fuel pellet and clad interior regions, the heat flow is governed by conduction,

where dz is the thickness of the axial interval where moderator flow related equations are solved, and k_i is the thermal conductivity [$\text{W}/\text{m}\cdot\text{K}$] evaluated at position \bar{r}_i . Special treatment should be made for outermost fuel pellet (\bar{r}_{N-2}) and clad (\bar{r}_N) faces, where heat flow is modelled as

$$Q_{N-2,N-1} = h_{gap}(\bar{T}_{N-2} - \bar{T}_{N-1}) \bullet 2\pi r_{N-2} \bullet dz, \quad (21)$$

$$Q_{N,N+1} = h_{fl}(\bar{T}_N - T_b) \bullet 2\pi r_N \bullet dz. \quad (22)$$

Notations h_{gap} and h_{fl} represent gap conductance [$\text{W}/\text{m}^2\cdot\text{K}$] and clad-to-bulk fluid heat transfer coefficients [$\text{W}/\text{m}^2\cdot\text{K}$] respectively. The value for h_{gap} is specified as an input, whereas h_{fl} is calculated based on the well-known Dittus-Boelter correlation.

$$h_{fl} = \left(\frac{k_{fl}}{D_h} \right) Nu, \quad (23)$$

The bulk fluid temperature (T_b) is pre-calculated as aforementioned, which serves as a boundary condition alongside adiabatic treatment of heat flow at the centre, i.e., $Q_{0,1} = 0$. Through implicit-Euler scheme and Eqs. (19)–(22), Eq. (18) reduces in to a tri-diagonal matrix in terms of temperature. The effective fuel temperature $T_{F,eff}$ is then calculated as

$$T_{F,eff} = 0.3\bar{T}_1 + 0.7\bar{T}_{N-2}. \quad (24)$$

To invoke the feedback effect, cross-sections for the material that comprises the reactor is adjusted in accordance with the change of TH variables as below:

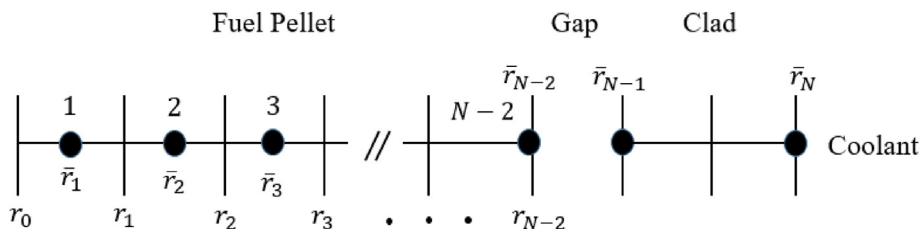


Fig. 2. Spatial discretization of a fuel rod.

$$\Sigma_{\alpha}(T_{F,eff}, T_M, D_M, Sb) = \Sigma_{\alpha,ref} + \frac{\partial \Sigma_{\alpha}}{\partial T_{F,eff}} \Delta \sqrt{T_{F,eff}} + \frac{\partial \Sigma_{\alpha}}{\partial T_M} \Delta T_M + \frac{\partial \Sigma_{\alpha}}{\partial D_M} \Delta D_M + \frac{\partial \Sigma_{\alpha}}{\partial Sb} \Delta Sb, \quad (25)$$

where T_M , D_M , and Sb denote moderator temperature, moderator density, and soluble boron density respectively. Note that the derivative terms are pre-evaluated from the lattice calculation [3].

2.5. Rod cusping issue

The transient processes involved in the operation of PWR often include the movement of control rods. Since the nodal calculation discretizes the reactor core into layers of nodes, the tip of the control rods may reside within the node during calculation. To reflect such a partially rodded condition, the macroscopic cross-section must be adjusted. The simplest approach is to volume weight the cross-sections according to the fraction of rod insertion, which is often referred to as volume-weighted cross-section (VWC) method.

$$\Sigma_{\alpha,g}^{PRN} = f_{in} \Sigma_{\alpha,g}^r + (1 - f_{in}) \Sigma_{\alpha,g}^u, \quad (26)$$

where f_{in} , $\Sigma_{\alpha,g}^r$, $\Sigma_{\alpha,g}^u$, and $\Sigma_{\alpha,g}^{PRN}$ represent a fraction of rod insertion, rodded cross-section, un-rodded cross-section, and estimated partially rodded cross-section value for reaction type α . Although straightforward, the VWC method overestimates $\Sigma_{\alpha,g}^{PRN}$ and manifests as an un-reliable power estimation, which is known as rod cusping problem.

To circumvent the cusping problem, KANT employs flux weighting cross-section (FWC) and neighborhood spectral index (NSI) methods [18,19]. In the FWC method, the average fluxes for rodded and un-rodded regions are estimated as

$$\phi_{g,k}^r = \frac{\Delta_{k+1} \phi_{g,k+1} + f_{in} \Delta_k \phi_{g,k}}{\Delta_{k+1} + f_{in} \Delta_k}, \quad \phi_{g,k}^u = \frac{\Delta_{k-1} \phi_{g,k-1} + (1 - f_{in}) \Delta_k \phi_{g,k}}{\Delta_{k-1} + (1 - f_{in}) \Delta_k}, \quad (27)$$

where $\phi_{g,k}$ is the flux obtained from global-balance equation with $\Sigma_{\alpha,g}^{PRN}$, and Δ_k denotes the axial node size. Note that node $k-1$ axially resides above node k . The cross-section for the rodded node is re-adjusted as

$$\Sigma_{\alpha,g}^{PRN} = \frac{f_{in} \Sigma_{\alpha,g}^r \phi_{g,k}^r + (1 - f_{in}) \Sigma_{\alpha,g}^u \phi_{g,k}^u}{f_{in} \phi_{g,k}^r + (1 - f_{in}) \phi_{g,k}^u}. \quad (28)$$

The overall scheme requires iteration, which is accommodated

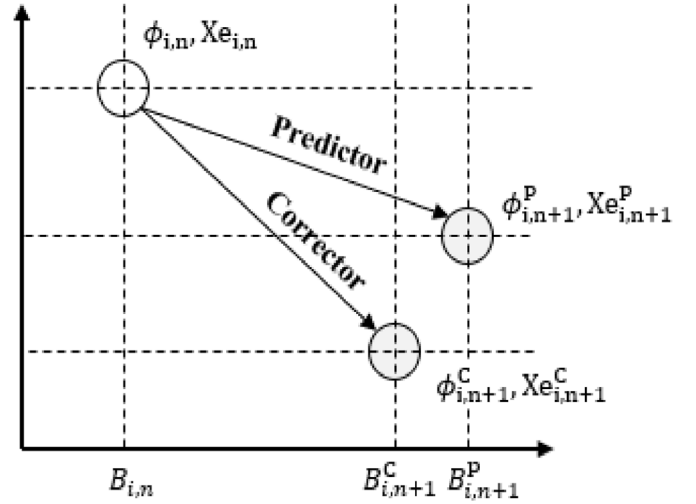


Fig. 4. Illustration of predictor-corrector scheme for macroscopic depletion calculation.

during neutron-balance calculation. The NSI method adjusts the fastest group ($g = 1$) cross-section in the same manner as FWC method, whereas the following calculation is performed for other groups:

$$\phi_{g,k}^r = \left(\frac{\phi_{g,k+1}}{\phi_{1,k+1}} \right) \bullet \phi_{1,k}^r, \quad \phi_{g,k}^u = \left(\frac{\phi_{g,k-1}}{\phi_{1,k-1}} \right) \bullet \phi_{1,k}^u. \quad (29)$$

2.6. Macroscopic depletion

The transmutation of nuclides subjected to nuclear reactions and radioactive decay can be modelled through the so-called Bateman equation, which is a system of first-order ODEs that can be readily solved through matrix operations [20]. However, implementation of such a method, also known as microscopic depletion, during whole core diffusion analyses could entail a noticeable computing burden. In lieu of considering transmutation of each isotope, homogenized assembly parameters can be pre-tabulated at each burnup point and directly utilized to perform macroscopic depletion.

For an accurate appraisal of Xenon-135 and Samarium-149 densities, simplified decay chains as shown in Fig. 3 are often considered together with the macroscopic depletion, where γ_i and λ_i denote yield and decay constant for isotope i respectively. Note that a concept of fictitious yield has been introduced for Samarium-149 (red colour),

and the yield values are adjusted to retain the reference number densities [21]. The corresponding set of simplified decay chain

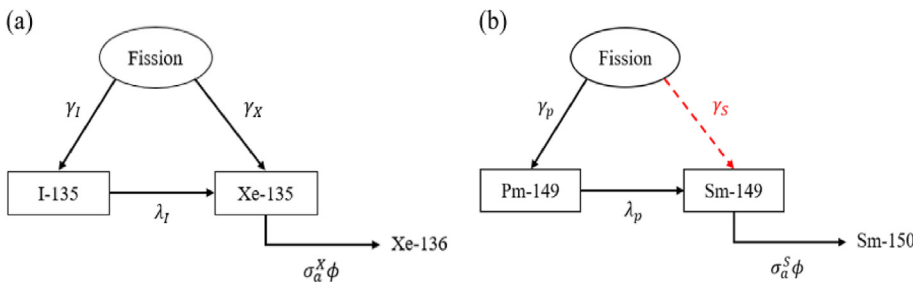


Fig. 3. Simplified decay chains for (a) Xenon-135 and (b) Samarium-149.

equations for Xenon-135 and Samarium-149 can be written as below:

Iodine-135 and Xenon-135.

$$\frac{dI}{dt} = \gamma_I \sum_{g=1}^G \Sigma_{fg} \phi_g(\mathbf{r}, t) - \lambda_I I(\mathbf{r}, t), \quad \frac{dX}{dt} = \gamma_X \sum_{g=1}^G \Sigma_{fg} \phi_g(\mathbf{r}, t) + \lambda_I I(\mathbf{r}, t) - \lambda_X X(\mathbf{r}, t) - \sum_{g=1}^G \sigma_{a,g}^X \phi_g(\mathbf{r}, t) X(\mathbf{r}, t), \quad (30)$$

Promethium-149 and Samarium-149.

$$\frac{dP}{dt} = \gamma_P \sum_{g=1}^G \Sigma_{fg} \phi_g(\mathbf{r}, t) - \lambda_P P(\mathbf{r}, t), \quad \frac{dS}{dt} = \lambda_P P(\mathbf{r}, t) - \sum_{g=1}^G \sigma_{a,g}^S \phi_g(\mathbf{r}, t) S(\mathbf{r}, t) + \gamma_S \sum_{g=1}^G \Sigma_{fg} \phi_g(\mathbf{r}, t), \quad (31)$$

where notations I , X , P , and S represent density for Iodine-135, Xenon-135, Promethium-149, and Samarium-149 respectively, and all the other notations are that of the convention.

Such simplified decay chains can be analytically solved by assuming constant flux and yield values, which are directly applied to the predictor-corrector scheme-based macroscopic depletion as shown in Fig. 4 [13]. Prediction is made for Xenon-135 and Samarium-149 concentrations (Xe_{n+1}^P) for the burnup step of interest ($n+1$) based on the known information (ϕ_n , Xe_n), and a steady-state calculation is performed to update the flux and power distribution (ϕ_{n+1}^P Xe_{n+1}^P). The simplified decay chains are once more calculated based on the updated flux and power distribution, adjusting the predicted poison concentrations (Xe_{n+1}^C). Applying the corrected poison information, the steady-state calculation can be solved once more correcting the flux and power distribution (ϕ_{n+1}^C Xe_{n+1}^C), hence attaining the name of the predictor-corrector scheme. It should be noted that the presence of the TH effect is subsumed during steady-state calculation.

When Xenon-135 and Samarium-149 are modelled, additional feedback terms must be included for the evaluation of absorption cross-section as below:

$$\Sigma_a(T_{F,eff}, T_M, D_M, Sb, P_0) = \Sigma_{a,ref} + \frac{\partial \Sigma_a}{\partial \sqrt{T_{F,eff}}} \Delta \sqrt{T_{F,eff}} + \frac{\partial \Sigma_a}{\partial T_M} \Delta T_M + \frac{\partial \Sigma_a}{\partial D_M} \Delta D_M + \frac{\partial \Sigma_a}{\partial Sb} \Delta Sb + N_{xe} \sigma_{a,xe} + N_{sm} \sigma_{a,sm} + \frac{\partial \Sigma_a}{\partial P_0} \Delta P_0 + \frac{1}{2} \frac{\partial^2 \Sigma_a}{\partial P_0^2} (\Delta P_0)^2 \quad (32)$$

where $N_{xe(sm)}$ and $\sigma_{a,xesm}$ represent the number density and microscopic absorption cross-section for Xenon-135 (Samarium-149), and P_0 denotes the node-wise power density in [W/cc]. Note that difference in the power density level affects the spectrum and

must be included during tabulation, which has a significant effect in macroscopic depletion calculation at early burnup steps [13]. The microscopic Xenon-135 and Samarium-149 cross-sections are

tabulated in an analogous manner to that of macroscopic cross-sections including the derivative terms.

2.7. Pin power reconstruction

As aforementioned, unless a pin-wise two-step procedure is employed, acquisition of localized pin power information requires certain assumption(s) due to assembly-wise homogenization process. The most intuitive approach is to directly utilize the form function (FF) which is pre-calculated during lattice calculation [10]:

$$FF(x, y) = \frac{P_{het}(x, y)}{P_{hom}(x, y)}, \quad (33)$$

where P_{het} and P_{hom} denote heterogeneous and homogeneous power (or flux) distribution in the fuel assembly. The homogeneous flux distribution can be calculated from either polynomial or analytic basis. In KANT, aside from the conventional reconstruction process using form function, a more sophisticated measure can be taken using the embedded pin power reconstruction (EPPR) method [22], although the current manuscript only includes the form function-based reconstruction result.

2.8. Flowchart for two-step calculation

Since the foremost motivation for developing KANT is to be employed for two-step analysis, it is noteworthy to include a

description of the overall two-step flowchart where the coupling scheme of KANT with lattice code(s) is demonstrated. Both the deterministic transport program DeCART2D and Monte Carlo-based transport program Serpent2 [4,23] can be utilized as a lattice code for KANT, where derivative terms enumerated in Eq. (32)

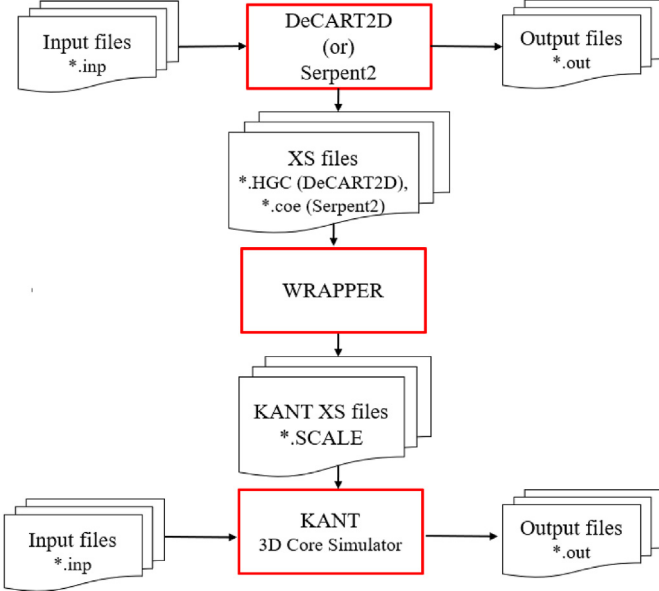


Fig. 5. Flowchart of DeCART2D (or Serpent2)/KANT two-step calculation procedure.

are evaluated through so-called branching calculation. Note that KANT uniquely considers the sensitivity related to power density variation and its effect in the depletion calculation is highlighted in the following section. Fig. 5 shows the overall two-step flowchart,

where the preprocessing code for tabulating lattice code output files for KANT simulation is named WRAPPER.

3. KANT benchmark verification

As aforementioned, KANT includes various calculation modules including steady and transient neutronics calculation, thermal-hydraulics (TH) feedback, GET-based nodal equivalence, macroscopic depletion, and pin power reconstruction. Whereupon, several benchmarks that require such module(s) have been solved for verification. For steady-state calculation, the IAEA 3-D PWR and 4-group KOEBERG problems have been considered [24,25]. To check the validity of handling rod cusping issue, a three-dimensional reflected reactor benchmark is solved [26]. For transient validation, calculation results for LMW-LWR [27] and NEACRP 3-D PWR benchmarks [28] are presented, where the latter problem models the TH feedback effect. To verify the macroscopic depletion and pin power reconstruction capacity, a small PWR problem modified with KAIST benchmark model [29] has been solved. For the overall validation of the multi-physics analysis capability of KANT, the BEAVRS cycle1 benchmark [30] has been investigated.

3.1. IAEA 3-D PWR and 4-group KOEBERG benchmarks

The IAEA 3-D PWR problem is a two-group three-dimensional standard benchmark for validating the performance of steady-state neutronics calculation methods. The reactor core is comprised of 177 fuel assemblies (including nine fully rodded and four partially rodded assemblies) and is surrounded by 64 reflector assemblies.

$\begin{array}{ccccccc} 0.7264 & 1.2742 & 1.4156 & 1.1884 & 0.6097 & 0.9524 & 0.9607 & 0.7798 \\ 0.7259 & 1.2736 & 1.4150 & 1.1879 & 0.6094 & 0.9519 & 0.9601 & 0.7788 \\ -0.07 & -0.05 & -0.04 & -0.04 & -0.05 & -0.05 & -0.06 & -0.13 \end{array}$ $\begin{array}{ccccccc} 1.3899 & 1.4248 & 1.2856 & 1.0685 & 1.0543 & 0.9764 & 0.9768 & 0.7600 \\ 1.3897 & 1.4243 & 1.2854 & 1.0681 & 1.0542 & 0.9764 & 0.9768 & 0.7591 \\ -0.01 & -0.04 & -0.02 & -0.04 & -0.01 & -0.04 & -0.04 & -0.12 \end{array}$ $\begin{array}{ccccccc} 1.3627 & 1.3065 & 1.1785 & 1.0888 & 1.0016 & 0.7152 & 0.7152 \\ 1.3623 & 1.3062 & 1.1782 & 1.0887 & 1.0011 & 0.7169 & 0.7169 \\ -0.03 & -0.02 & -0.03 & -0.03 & -0.01 & -0.05 & -0.24 \end{array}$ $\begin{array}{ccccccc} 1.1751 & 0.9702 & 0.9238 & 0.8698 & & & \\ 1.1750 & 0.9699 & 0.9241 & 0.8711 & & & \\ -0.01 & -0.03 & -0.03 & 0.03 & 0.15 & & \\ & & & & & 0.6017 & \\ & & & & & 0.6050 & \\ & & & & & 0.55 & \end{array}$ PARCS KANT Relative Error [%]	$\begin{array}{ccccccc} 1.0053 & 1.0856 & 1.0440 & 1.1638 & 1.1316 & 1.2148 & 0.9595 & 0.8334 \\ 1.0062 & 1.0862 & 1.0449 & 1.1642 & 1.1322 & 1.2145 & 0.9599 & 0.8322 \\ 0.09 & 0.06 & 0.08 & 0.03 & 0.05 & 0.03 & 0.04 & -0.14 \end{array}$ $\begin{array}{ccccccc} 1.0259 & 1.1303 & 1.1051 & 1.2430 & 1.0616 & 1.0424 & 0.6426 \\ 1.0267 & 1.1308 & 1.1058 & 1.2428 & 1.0620 & 1.0419 & 0.6417 \\ 0.08 & 0.04 & 0.06 & -0.02 & 0.04 & -0.05 & -0.15 \end{array}$ $\begin{array}{ccccccc} 1.0925 & 1.2235 & 1.0579 & 1.0392 & 0.9687 & & \\ 1.0933 & 1.2235 & 1.0585 & 1.0394 & 0.9673 & & \\ 0.07 & 0.00 & 0.05 & 0.02 & -0.14 & & \\ & & 1.0361 & 0.9989 & 0.9815 & 0.6506 & \\ & & 1.0367 & 0.9992 & 0.9810 & 0.6497 & \\ & & 0.06 & 0.03 & -0.05 & -0.14 & \\ & & & & 0.7862 & 0.6673 & \\ & & & & 0.7867 & 0.6663 & \\ & & & & 0.06 & -0.15 & \end{array}$ 4x4 ANM KANT Relative Error [%]
---	---

Fig. 6. Relative error of radial power densities for (a) IAEA 3-D and (b) 4-group KOEBERG benchmarks.

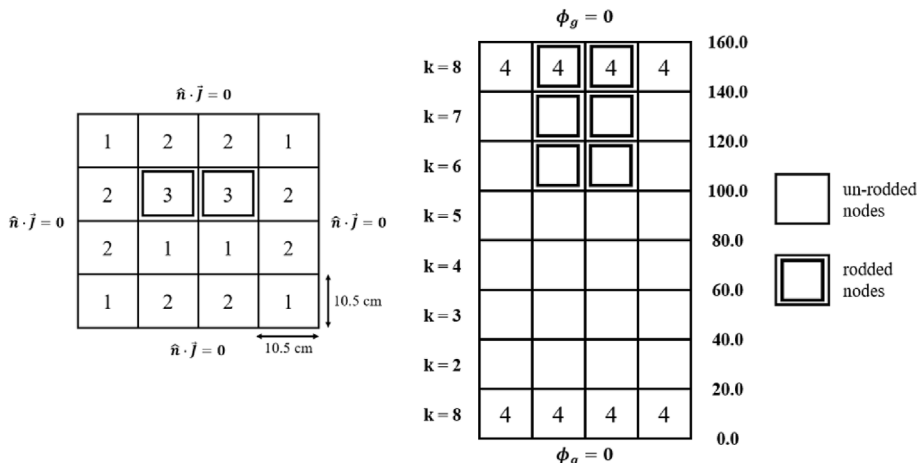


Fig. 7. Benchmark for correction of rod cusping issue.

Table 1

Multiplication factors for IAEA 3-D and 4-group KOEBERG benchmarks.

IAEA 3-D benchmark		Node Size (cm ³)	Multiplication Factor
Computer Code			
PARCS		20 × 20 × 20	1.029096
KANT		10 × 10 × 20	1.029097
4-group KOEBERG benchmark		Node Size (cm ²)	Multiplication Factor
Computer Code		5.402 × 5.402	1.007962
4 × 4 ANM		5.402 × 5.402	1.007952
KANT			

Table 2

Material properties for rod cusping benchmark.

type	group	D _g (cm)	Σ _{fg} (cm ⁻¹)	Σ _{s,g' → g} (cm ⁻¹)	νΣ _{fg} (cm ⁻¹)
1	1	1.5134	0.03322	0.02113	0.006011
	2	0.3951	0.16866	0.0	0.199070
2	1	1.5133	0.03045	0.02112	0.004625
	2	0.3951	0.14128	0.0	0.164310
3	1	1.4659	0.03648	0.01895	0.006029
	2	0.3833	0.20765	0.0	0.202460
4	1	1.70	0.036	0.035	0.0
	2	0.35	0.050	0.0	0.0

$$\nu = 2.5$$

$$\chi_1 = 1.0, \chi_2 = 0.0$$

Table 3

Delayed neutron data for rod cusping benchmark.

Precursor Group	β _k	λ _k
1	0.000247	0.0127
2	0.0013845	0.0317
3	0.001222	0.115
4	0.0026455	0.311
5	0.000832	1.40
6	0.000169	3.87

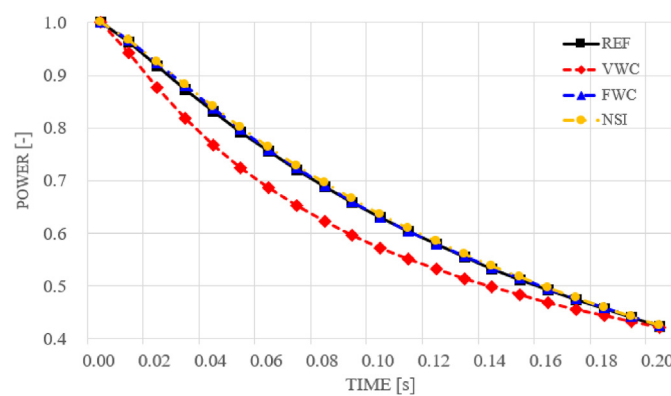


Fig. 8. Calculation result for rod cusping benchmark.

The reference solution was taken from PARCS calculation with a node size of 20 cm × 20 cm × 20 cm. The KANT calculation was performed with a node size of 10 cm × 10 cm × 20 cm, where the acquired power density was condensed whilst retaining the assembly-wise reaction rate for comparison. Since it is well-known

Table 4

Comparison of initial multiplication factor for LMW-LWR benchmark.

Computer Code	Node Size (cm ³)	Multiplication Factor
KANT	10 × 10 × 10	0.99970
POLCA7	20 × 20 × 20	0.99970
QUANDRY	20 × 20 × 20	0.99974
AETNA	10 × 10 × 5	0.99971
SPANDEX	5 × 5 × 2	0.99964

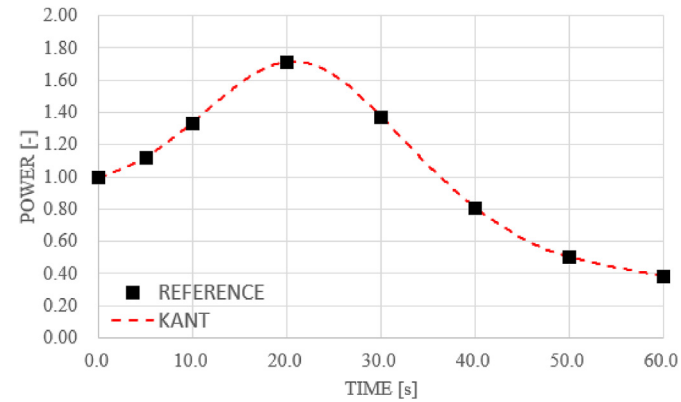


Fig. 9. Calculated power evolution for LMW-LWR benchmark.

Table 5

Evaluated power during transient for LMW-LWR benchmark.

Time (s)	QUANDRY	KANT	Relative Error (%)
0.0	1.000	1.000	0.0
5.0	1.121	1.127	0.6
10.0	1.331	1.341	0.7
20.0	1.713	1.714	0.0
30.0	1.368	1.375	0.5
40.0	0.806	0.811	0.6
50.0	0.499	0.504	1.1
60.0	0.383	0.387	1.1

that assembly-wise NEM calculation result often lacks enough accuracy, each assembly has been divided into a 2 × 2 configuration. The relative error throughout this work is defined as

$$ERR(\%) = \left(\frac{P_{ref} - P_{KANT}}{P_{ref}} \right) \times 100. \quad (34)$$

For validation of the multigroup nodal calculation with a group number larger than two, a four-group two-dimensional KOEBERG benchmark has been considered. It models the beginning of life core of Unit 1 of the KOEBERG nuclear power station, which consists of 157 fuel assemblies of three enrichments and three different burnable absorber loadings. The reference calculation was taken

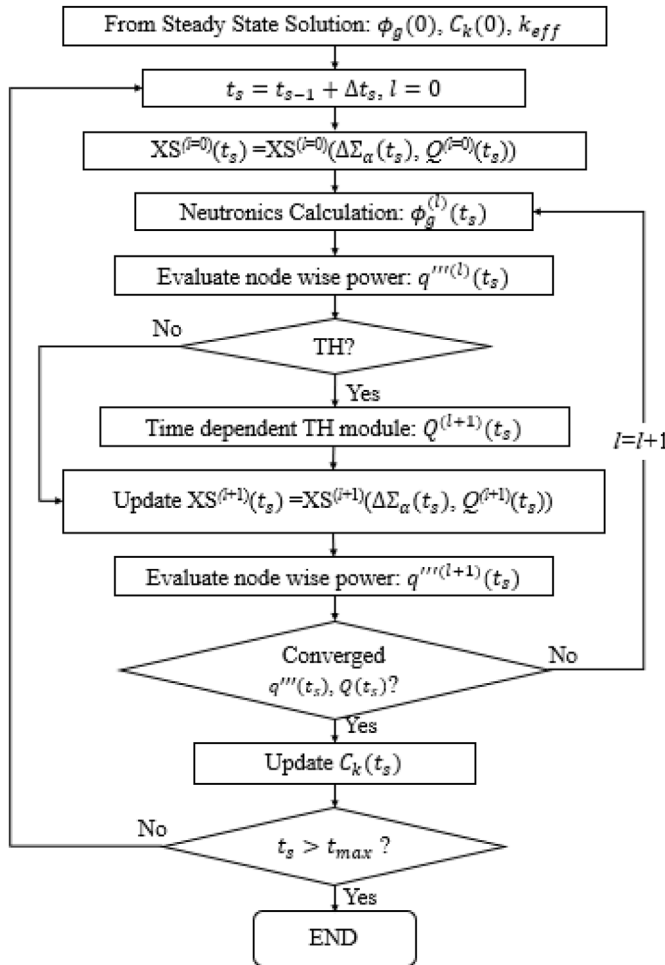


Fig. 10. Multi-physics transient calculation flowchart of KANT.

from the 4×4 ANM (Analytic Nodal Method) calculation [25], and KANT calculation was performed under the same condition.

Fig. 6 depicts the radial power density distributions and Table 1 compares the multiplication factors for two benchmarks. The deviation in the eigenvalue was below 1.0 pcm, and the power density profiles well resemble each other, which altogether validates the steady-state neutronics calculation of KANT.

3.2. Benchmark for correction of rod cusping issue

As discussed, for accurate transient calculation, rod cusping issue must be resolved, where KANT employs FWC or NSI methods for correction. To validate the accuracy of such corrections, the following simple three-dimensional benchmark has been solved [26]. Fig. 7 illustrates the horizontal and vertical sections of the benchmark reactor, and Tables 2 and 3 enumerate the material properties and delayed neutron data respectively. $v_1 = 1.25 \times 10^7 \text{ cm/s}$, $v_2 = 2.5 \times 10^5 \text{ cm/s}$.

The control rod bank is initially positioned at $z = 100 \text{ cm}$, and is inserted at a rate of 100 cm/s for 0.2 s . The reference solution has been calculated with a time-step of 0.01 s and axial node size of 1 cm to prevent any cusping, i.e., the nodes are either fully rodded or un-rodded during calculation. To test the validity of correction schemes, the same calculation was performed with an enlarged axial node size of 20 cm . Fig. 8 exhibits the evaluated power from each case, where both FWC and NSI methods are applicable for rod

Table 6
Calculation result for NEACRP 3-D PWR benchmark.

Case	A1	A2	B1	B2	C1	C2
Core Condition	HZP	HFP	HZP	HFP	HZP	HFP
Critical boron (ppm)						
PANTHER (1993)	567.7	1160.6	1254.6	1189.4	1135.3	1160.6
PANTHER (1997)	561.2	1156.6	1248.0	1183.8	1128.3	1156.6
KANT	561.5	1156.6	1251.5	1184.0	1131.6	1156.6
Time of power peak (s)						
PANTHER (1993)	0.560	0.100	0.520	0.120	0.270	0.100
PANTHER (1997)	0.538	0.095	0.523	0.100	0.271	0.095
KANT	0.540	0.093	0.497	0.098	0.264	0.096
Power peak [-]						
PANTHER (1993)	1.18	1.080	2.44	1.063	4.77	1.071
PANTHER (1997)	1.27	1.083	2.32	1.064	4.41	1.073
KANT	1.19	1.081	2.45	1.066	4.34	1.075
Final power [-]						
PANTHER (1993)	0.196	1.035	0.320	1.038	0.146	1.030
PANTHER (1997)	0.197	1.036	0.320	1.039	0.146	1.031
KANT	0.197	1.035	0.322	1.040	0.148	1.032
Final average fuel temperature (°C)						
PANTHER (1993)	324.3	554.6	349.9	552.0	315.9	553.5
PANTHER (1997)	324.9	555.2	350.0	552.4	315.9	553.5
KANT	324.6	550.7	350.2	548.6	316.0	550.0
Final coolant outlet temperature (°C)						
PANTHER (1993)	293.1	324.6	297.6	324.7	291.5	324.5
PANTHER (1997)	293.2	324.9	297.7	324.8	291.7	324.6
KANT	293.2	325.2	297.9	325.3	291.6	325.1

cusping correction.

3.3. LMW-LWR benchmark

The LMW-LWR benchmark is a two-group three-dimensional transient neutronics benchmark that includes control rod movement. The reactor core consists of 77 fuel assemblies and is surrounded by water reflector regions. The pitch of each assembly is 20 cm and the total height of the core is 200 cm . Two different control rod banks are considered in the benchmark. Note that feedback effect is not modelled in this benchmark.

At the onset of transient, a partially inserted control rod bank is withdrawn about 80 cm to its fully withdrawn position with a rate of 3 cm/s . After 7.5 s from the onset of transient, insertion of the additional control rod bank from the fully withdrawn position is initiated with a rate of 3 cm/s with a time duration of 40 s . The detailed core description and material properties can be found in reference [27]. To minimize the rod cusping effect, the FWC method has been utilized during KANT calculation with a time step of 125 ms and node size of $10 \text{ cm} \times 10 \text{ cm} \times 10 \text{ cm}$.

Note that NEM calculation requires at least 2×2 assembly division for accurate evaluation. The calculated initial multiplication factor is presented and compared with various nodal codes in Table 4 [31]. Estimated power variation during transient is represented in Fig. 9 and Table 5, where the reference solution was taken from QUANDRY [32]. Both the initial eigenvalue and the power evolution from the KANT calculation well match that of the reference.

3.4. NEACRP 3-D PWR benchmark

The NEACRP 3-D PWR benchmark is a two-group three-dimensional reactor problem that mimics the geometry and operation conditions of a typical PWR. The reactor core is comprised of 157 fuel assemblies and is surrounded by reflector assemblies. Such a benchmark specifies the thermal-hydraulics (TH) feedback effect including the soluble boron, which demands both an accurate neutronics solver and a proper TH-model alongside a coupling

0.9931	1.5208	1.0711	1.8070	1.8151	1.0075	0.3961	0.5402
0.9891	1.5150	1.0668	1.8000	1.8077	1.0053	0.3982	0.5475
-0.40	-0.38	-0.40	-0.39	-0.41	-0.22	0.53	1.35
1.8451	1.6614	1.9113	1.4245	0.5588	0.5600	0.4279	
1.8389	1.6550	1.9041	1.4199	0.5588	0.5626	0.4348	
-0.34	-0.39	-0.38	-0.32	0.00	0.46	1.61	
1.0149	1.4483	0.7302	0.7257	0.3822			
1.0115	1.4444	0.7296	0.7269	0.3851			
-0.34	-0.27	-0.08	0.17	0.76			
1.4350	1.0162	0.9453	0.5406				
1.4345	1.0175	0.9510	0.5475				
-0.03	0.13	0.60	1.28				
PARCS		0.5421	0.6709				
KANT		0.5452	0.6789				
Relative Error [%]		0.57	1.19				

0.9155	1.0243	1.1546	1.1192	1.1773	1.1299	0.8508	0.7323
0.9027	1.0145	1.1438	1.1122	1.1711	1.1273	0.8505	0.7422
-1.40	-0.96	-0.94	-0.63	-0.53	-0.23	-0.04	1.35
1.1241	1.1698	1.1893	1.1544	1.0914	0.9496	0.5806	
1.1127	1.1608	1.1811	1.1499	1.0895	0.9537	0.5918	
-1.01	-0.77	-0.69	-0.39	-0.17	0.43	1.93	
1.2002	1.1720	1.1304	1.0109	0.9147			
1.1906	1.1661	1.1267	1.0132	0.9247			
-0.80	-0.50	-0.33	0.23	1.09			
1.1386	1.0325	0.9794	0.6426				
1.1341	1.0334	0.9855	0.6558				
-0.40	0.09	0.62	2.05				
PARCS		0.9111	0.7086				
KANT		0.9167	0.7221				
Relative Error [%]		0.61	1.91				

(a) NEACRP-A1 [HZP]

(b) NEACRP-A2 [HFP]

Fig. 11. Calculated radial power density distributions for (a) NEACRP case A1 and (b) NEACRP base A2.

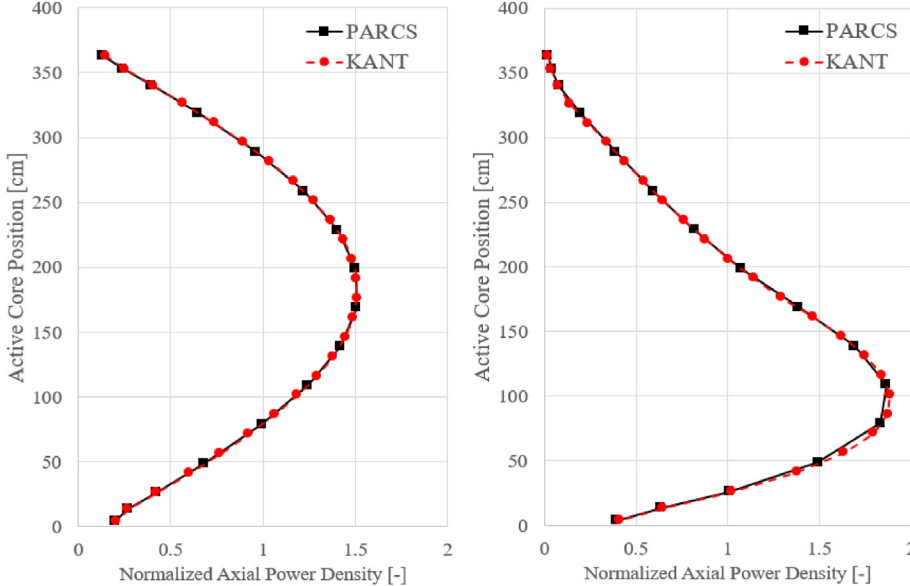


Fig. 12. Calculated axial power density distributions for (a) NEACRP case A1 and (b) NEACRP base A2.

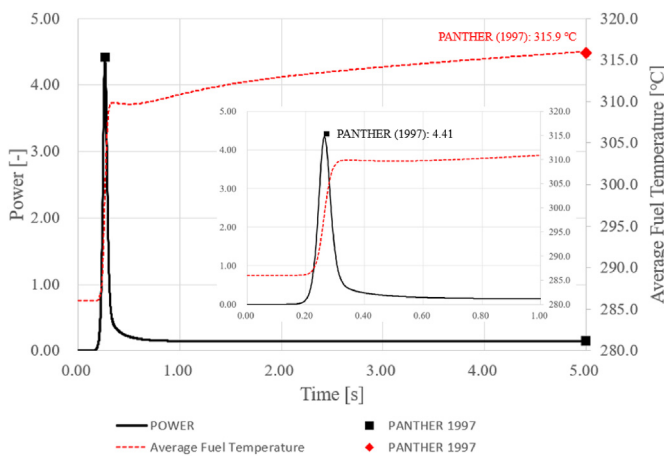


Fig. 13. KANT Calculation result for NEACRP case C1.

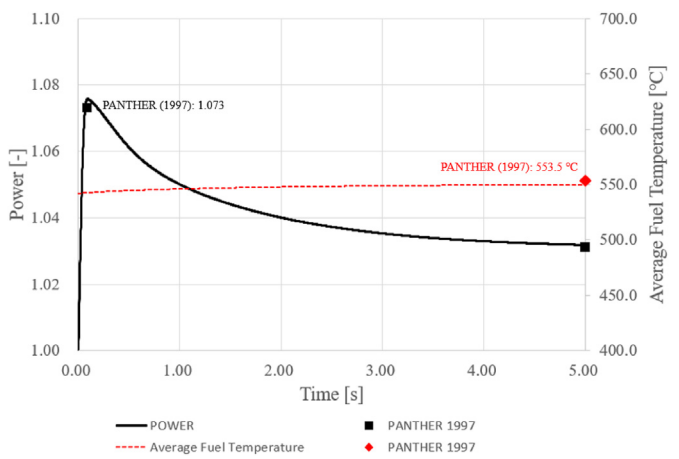


Fig. 14. KANT Calculation result for NEACRP case C2.

scheme to attain a reasonable solution. Hence, it is regarded as one of the most important benchmarks for validating a multi-physics reactor simulator. The overall flowchart of KANT multi-physics transient calculation module is represented in Fig. 10, where Q denotes the thermal-hydraulics related variables, super-script l is

the iteration index, and all the other notations are that of the convention.

The rated hot-full-power (HFP) of the NEACRP core is 2775 MWth and the hot-zero-power (HZP) condition postulates a 0.01% power level of HFP. Three different transient scenarios are

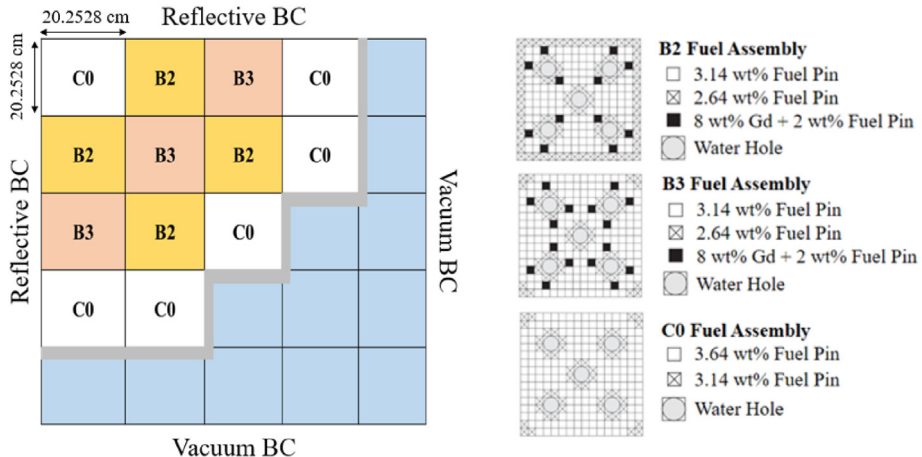


Fig. 15. Layout for small PWR problem based on KAIST benchmark.

*ASSEMBLY WISE					*PPR RESULT				
3.311	1.565	0.814	0.608		5.309	6.903	6.275	6.676	
3.333	1.563	0.806	0.613	DeCART2D KANT (2x2)	1.279	1.767	1.773	1.722	MAX (%)
0.7	-0.2	-1.0	0.8	ERROR [%]	6.084	6.633	21.239		RMS (%)
1.036	0.661	0.432			1.944	1.641	3.070		
1.024	0.660	0.433						17.862	
-1.1	-0.1	0.3							2.975
	0.493								
	0.493								
	-0.1								

(a) (b)

Fig. 16. Whole core nodal calculation result using KANT for (a) assembly-wise power density and (b) pin power reconstructed result.

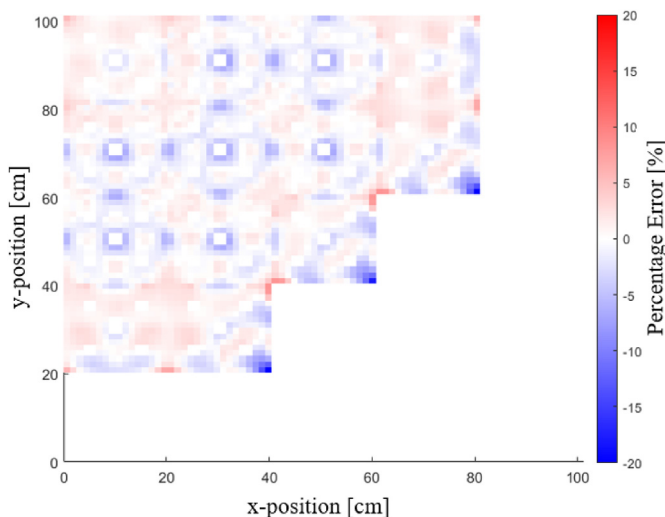


Fig. 17. Pin-wise reconstructed pin power error.

simulated for HZP (A1, B1, C1) and HFP (A2, B2, C2) conditions, which are initiated by the ejection of a control rod from the core. Critical boron concentration, time of power peak, power peak level, final power level, final average fuel and moderator temperatures are tabulated for comparison. Further detailed description can be found in reference [28].

It has been a convention to regard either the original (1993) or the refined (1997) PANTHER solutions to be reference [33]. The simulation results from two-different PANTHER calculations for

HFP condition, e.g., A2, B2, and C2, well resemble each other. However, some noticeable discrepancies can be found for transient scenarios for HZP condition, e.g., A1, B1, and C1. Especially, it has been reported that several computing code solutions conspicuously vary from each other for HZP simulations, where the deviation could reach more than 20% [34].

The NEACRP 3-D benchmark solution obtained from KANT utilized a very fine time-step of 1 ms for an accurate evaluation. Each assembly of the reactor was divided into four equally sized nodes, i.e., 2×2 spatial discretization for each assembly. Table 6 enumerates the calculated result using KANT alongside 1993 and 1997 PAHTER results for comparison.

It is worthwhile to articulate that converged steady-state solution for NEACRP benchmark is a prerequisite to perform TH-coupled multi-physics transient calculation. Hence, the given problem naturally presents a validation for TH coupled multi-physics steady-state calculation. For the determination of steady-state, the critical boron concentration (CBC) must be evaluated, where the CBC values using KANT are generally accurate, exhibiting a maximum deviation of about 0.29% with respect to PANTHER 1997 that occurred in case C1. Figs. 11 and 12 depict the radial and axial normalized power density distributions obtained from PARCS and KANT for comparison, where reasonable agreement can be seen between the two different codes [35].

The final power, average fuel temperature, and coolant outlet temperature from KANT well resemble both of the PANTHER results for all cases. In addition, the disparities for the time of power peak and its level were less than 2 ms and 0.2% respectively for HFP simulations between KANT and PANTHER 1997 solutions.

For HZP simulation results, relatively large differences can be observed for both the time of power peak and its level. However,

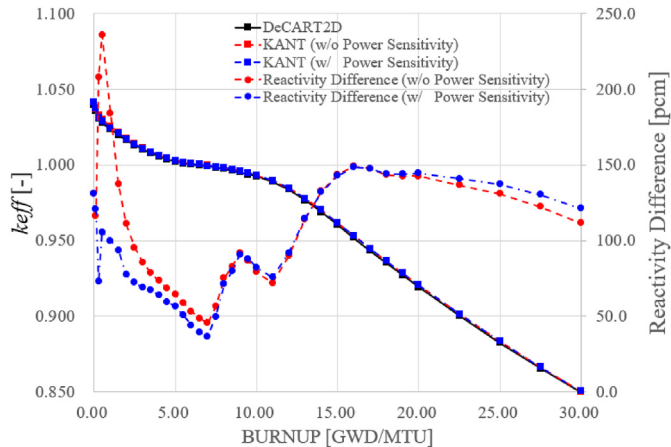


Fig. 18. Macroscopic depletion result and its associated reactivity difference.

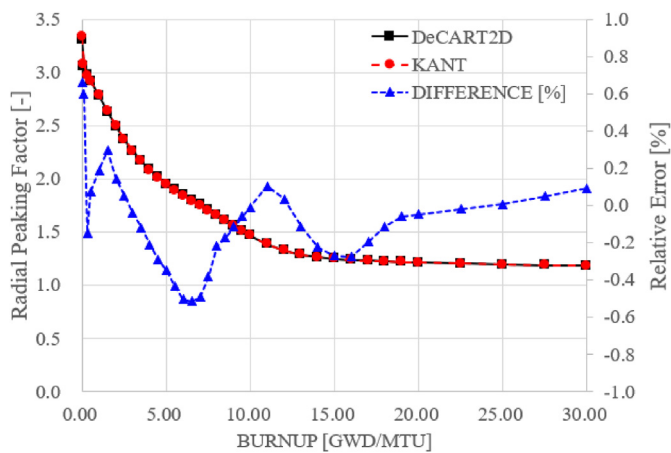


Fig. 19. Evolution of radial peaking factor and its relative difference (error).

the extent of such differences is tantamount or less compared to the reported deviation among various nodal codes. Figs. 13 and 14 demonstrate the power evolutions for case C1 and C2, where PANTHER 1997 results are marked for comparison.

3.5. Small PWR problem based on KAIST benchmark model

A small PWR problem based on KAIST benchmark has been considered for testing the macroscopic depletion and pin power reconstruction capability of KANT as shown in Fig. 15 [22,29]. Three different types of 16×16 fuel assemblies comprise the core and are surrounded by baffle reflectors. Both lattice and whole-core calculations have been performed using the two-dimensional deterministic transport code DeCART2D for the generation of homogenized cross-sections and reference solutions respectively [4]. Note that discontinuity factors and form function are also tabulated from the lattice calculation and applied during macroscopic depletion calculation.

The reference multiplication factor from the whole core transport calculation is 1.07292, and the KANT-based whole core 2×2 nodal calculation is 1.07624 exhibiting a reactivity difference of about 114 pcm, which is a typical error for a two-step analysis. Note that lattice calculation based homogenized cross-sections and discontinuity factors have been employed. Fig. 16 compares the assembly-wise power densities, which shows reasonable agreement, and the error of form function (FF) based pin power

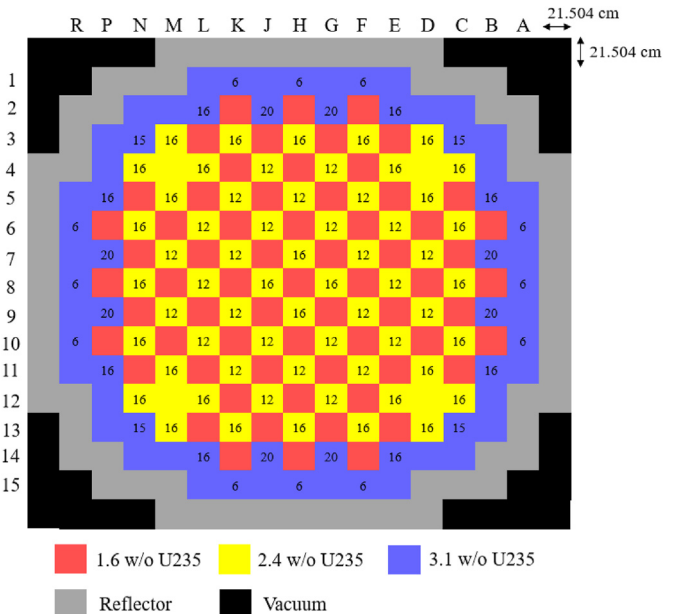


Fig. 20. Radial core layout for BEAVRS benchmark Cycle 1.

reconstruction result is shown in Fig. 17. One could recognize that noticeable discrepancies are only localized at the fringe of the active core region facing the baffle reflectors, where the absolute power density is relatively low.

The assembly-wise maximum and root-mean-square (RMS) errors for reconstructed pin power are shown in Fig. 16 where the RMS error (percent) in this manuscript is defined as below:

$$\text{RMS Error (\%)} = \sqrt{\frac{1}{n} \sum_{i=1}^n \left(\frac{v_i^{\text{predicted}} - v_i^{\text{ref}}}{v_i^{\text{ref}}} \times 100 \right)^2}, \quad (35)$$

where $v_i^{\text{predicted}}$ is the predicted quantity, v_i^{ref} is the reference quantity, and n is the number of predictions considered.

As aforementioned, for an accurate evaluation of Xenon-135 and Samarium-149 densities and their neutronics effect, yield values have been corrected for the simplified decay chain models used in predictor-corrector-based macroscopic depletion. In addition, derivative terms with respect to the assembly-wise power density, i.e., power density sensitivity, have been included to reflect variation in the neutron spectrum. Fig. 18 depicts the whole core depletion result and reactivity differences, where noticeable improvement can be observed at the early burnup steps with inclusion of power sensitivity. The evolution of corresponding radial peaking factor whilst including the power sensitivity is shown in Fig. 19, where the relative error with respect to the transport calculation is also exhibited for comparison. Note that equilibrium Xenon-135 and Samarium-149 densities have been postulated for each burnup step.

3.6. BEAVRS Cycle1 benchmark

The BEAVRS benchmark specification was published by the Massachusetts Institute of Technology (MIT) Computational Reactor Physics Group in 2013 and has undergone several updates [30]. The benchmark specification provides a detailed description of a 4-loop Westinghouse nuclear reactor having a power level of 3411 MWth. It includes thorough information pertaining to the hot

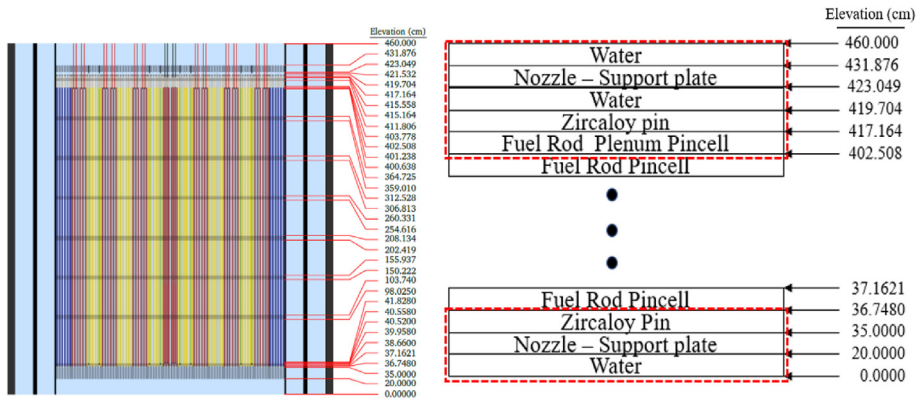


Fig. 21. Axial core layout for BEAVRS.

Table 7
Nominal values for the HFP condition.

Item	Value	Units
Total Power	3411	[MWth]
Core Pressure	155.17	[bar]
Inlet Temperature	292.78	[°C]
Outlet Temperature	310	[°C]
Mass Flow Rate	17,083	[kg/s]
Initial Heavy Metal	81.8	[ton]

Table 8
Fuel assembly geometry information.

Item	Value	Units
Active Core Height	365.76	[cm]
Assembly Pitch	21.504	[cm]
Number of Fuel Rods	264	[–]
Number of Guide Tube Rods	25	[–]
Fuel Rod Diameter	7.84	[mm]
Cladding Inner Diameter	8.00	[mm]
Cladding Outer Diameter	9.14	[mm]
Guide Tube Inner Diameter	11.22	[mm]
Guide Tube Outer Diameter	12.04	[mm]
Pin Pitch	12.60	[mm]

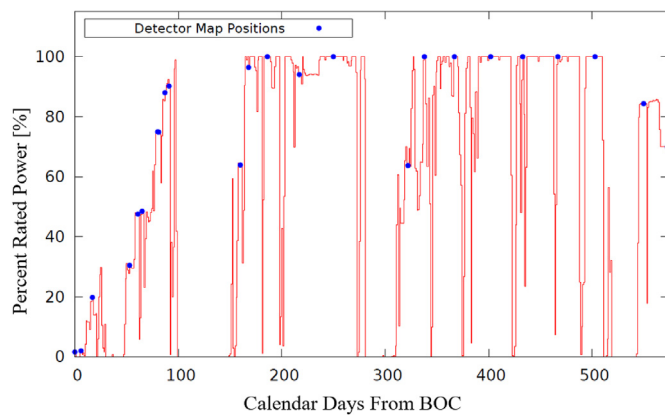


Fig. 22. Power histories of BEAVRS benchmark for Cycle 1.

zero power (HZP) measurements and reactor operating conditions for the first and second fuel cycles. Fig. 20 depicts the overall radial core layout of the BEAVRS Cycle1 benchmark, where the number of burnable absorbers and enrichment for each fuel assembly are

Table 9
Branching calculation conditions.

Type	Reference	High	Low
Boron Concentration [ppm]	0	1000	500
Fuel Temperature [K]	900	1200	600
Moderator Temperature [K]	575	590	560
Moderator Density [g/cc]	0.7227	0.7521	0.6883

Table 10
Calculated critical boron concentration at HZP.

Parameter	Critical Boron Concentration [ppm]		
	BEAVRS	KANT	Difference
HZP (ARO)	975	979.94	4.94

given. Fig. 21 illustrates the axial description of the problem, where homogenization of axial layouts for top and bottom regions excluding the active core is marked with a red-coloured box. Note that the benchmark given axial core description includes fuel spacers; however, it was omitted in the homogenized assembly models for two-step analysis [7]. Nominal values for the HFP condition are tabulated in Table 7, and Table 8 enumerates the overall geometry of the fuel assembly. The power operation history for BEAVRS Cycle 1 is given in Fig. 22, and a further description of the problem can be found in reference [30].

The lattice calculation for generating burnup-dependent macroscopic cross-sections and various derivative terms was conducted using the Serpent Version 2.131 continuous energy Monte Carlo transport program [23] and ENDF/B-VII.1 data library. The power density was set to be 100% HFP condition with the following nominal state values:

- Boron Concentration: 0 ppm
- Fuel Temperature: 900 [K]
- Moderator Temperature: 575 [K]
- Moderator Density: 0.7227 [g/cc]

The branching calculation conditions for assessing the various derivative terms are listed in Table 9. Note that all the calculation was performed with 60 inactive, and 260 active cycles with 200,000 histories per cycle. From the acquired Xenon-135 and Samarium-149 concentrations under 100% power density condition, the yield values have been adjusted as discussed in Section 2.6. Note that power density-related derivative terms have been omitted for the presented analysis.

	H	G	F	E	D	C	B	A
8		0.779	1.065	0.940	1.147	0.935	1.264	0.778
	0.914 (-)	0.705 (-9.5)	1.051 (-1.3)	0.881 (-6.3)	1.173 (2.2)	0.905 (-3.2)	1.350 (6.8)	0.822 (5.6)
	0.932 (-)	0.713 (-8.4)	1.065 (-0.2)	0.887 (-5.7)	1.180 (2.8)	0.906 (-3.1)	1.352 (6.9)	0.825 (6.0)
9	0.779	1.011	0.897	1.143	0.974	1.168	0.873	0.815
	0.705 (-9.5)	0.999 (-1.2)	0.842 (-6.1)	1.146 (0.3)	0.928 (-4.7)	1.240 (6.2)	0.857 (-1.8)	0.865 (6.1)
	0.713 (-8.4)	1.011 (0.0)	0.849 (-5.3)	1.157 (1.2)	0.933 (-4.2)	1.245 (6.6)	0.855 (-2.1)	0.866 (6.2)
10	1.065	0.897	1.138	0.968	1.212	0.984	1.242	0.728
	1.052 (-1.2)	0.842 (-6.1)	1.137 (-0.1)	0.968 (-4.0)	1.227 (1.3)	0.938 (-4.7)	1.337 (7.8)	0.765 (5.1)
	1.063 (-0.2)	0.849 (-5.3)	1.147 (0.8)	0.936 (-3.3)	1.235 (1.9)	0.940 (-4.5)	1.333 (7.3)	0.761 (4.6)
11	0.940	1.143	0.968	1.249	-	1.307	-	0.584
	0.881 (-6.3)	1.147 (0.4)	0.930 (-4.0)	1.268 (1.6)	0.995 (-)	1.394 (6.7)	0.887 (-)	0.616 (5.4)
	0.887 (-5.7)	1.157 (1.2)	0.936 (-3.3)	1.278 (2.3)	1.002 (-)	1.398 (7.0)	0.880 (-)	0.611 (4.7)
12	1.147	0.974	1.212	-	1.343	1.196	0.958	
	1.174 (2.3)	0.929 (-4.6)	1.228 (1.3)	0.996 (-)	1.365 (1.6)	1.101 (-7.9)	0.963 (0.5)	
	1.180 (2.8)	0.933 (-4.2)	1.235 (1.9)	1.002 (-)	1.381 (2.8)	1.101 (-7.9)	0.958 (0.0)	
13	0.935	1.168	0.984	1.307	1.196	0.852	0.702	
	0.906 (-3.1)	1.242 (6.3)	0.939 (-4.6)	1.395 (6.7)	1.101 (-7.9)	0.917 (7.7)	0.682 (-2.8)	
	0.906 (-3.1)	1.245 (6.6)	0.940 (-4.5)	1.398 (7.0)	1.101 (-7.9)	0.910 (6.8)	0.688 (-2.0)	
14	1.264	0.873	1.242	-	0.958	0.702		
	1.353 (7.1)	0.859 (-1.6)	1.339 (7.8)	0.888 (-)	0.963 (0.5)	0.683 (-2.8)		
	1.352 (6.9)	0.855 (-2.1)	1.333 (7.3)	0.880 (-)	0.958 (0.0)	0.688 (-2.0)		
15	0.778	0.815	0.728	0.584				
	0.825 (6.0)	0.868 (6.5)	0.767 (5.3)	0.617 (5.6)				
	0.825 (6.0)	0.866 (6.2)	0.761 (4.6)	0.611 (4.7)				
BEAVRS PARCS (%) KANT (%)								

Fig. 23. Radial thermal flux distribution for BEAVRS Cycle1.

	H	G	F	E	D	C	B	A
8	0.709	0.801	0.804	0.971	0.872	0.966	0.939	1.004
	0.668 (-5.7)	0.752 (-6.1)	0.769 (-4.4)	0.932 (-4.0)	0.857 (-1.7)	0.965 (-0.1)	0.991 (5.5)	1.094 (8.9)
	0.680 (-4.1)	0.760 (-5.1)	0.775 (-3.6)	0.937 (-3.5)	0.860 (-1.3)	0.966 (-0.1)	0.989 (5.3)	1.094 (8.9)
9	0.801	0.767	0.938	0.868	1.007	0.900	1.133	1.065
	0.752 (-6.1)	0.731 (-4.8)	0.891 (-5.0)	0.838 (-3.4)	0.983 (-2.4)	0.908 (0.9)	1.167 (3.0)	1.143 (7.3)
	0.760 (-5.1)	0.737 (-3.9)	0.898 (-4.3)	0.843 (-2.9)	0.986 (-2.1)	0.909 (1.0)	1.162 (2.6)	1.142 (7.2)
10	0.804	0.938	0.864	1.022	0.913	1.010	0.941	0.939
	0.769 (-4.4)	0.891 (-5.0)	0.831 (-3.9)	0.984 (-3.7)	0.897 (-1.8)	1.001 (-0.9)	0.980 (4.2)	1.017 (8.3)
	0.775 (-3.6)	0.898 (-4.3)	0.836 (-3.2)	0.989 (-3.3)	0.901 (-1.4)	1.001 (-0.9)	0.976 (3.7)	1.010 (7.5)
11	0.971	0.868	1.022	0.951	1.095	1.024	1.187	0.779
	0.933 (-4.0)	0.839 (-3.4)	0.984 (-3.7)	0.928 (-2.5)	1.065 (-2.8)	1.021 (-0.3)	1.198 (0.9)	0.815 (4.6)
	0.937 (-3.5)	0.843 (-2.9)	0.989 (-3.3)	0.932 (-2.0)	1.070 (-2.3)	1.021 (-0.3)	1.188 (0.1)	0.808 (3.7)
12	0.872	1.007	0.913	1.095	1.444	1.193	1.269	
	0.858 (-1.6)	0.983 (-2.3)	0.898 (-1.7)	1.065 (-2.7)	1.427 (-1.2)	1.186 (-0.6)	1.271 (0.2)	
	0.860 (-1.3)	0.986 (-2.1)	0.901 (-1.4)	1.070 (-2.3)	1.442 (-0.2)	1.184 (-0.7)	1.264 (-0.4)	
13	0.966	0.900	1.010	1.024	1.193	1.250	0.936	
	0.967 (0.1)	0.909 (1.0)	1.002 (-0.8)	1.021 (-0.3)	1.186 (-0.6)	1.247 (-0.3)	0.904 (-3.4)	
	0.966 (-0.1)	0.909 (1.0)	1.001 (-0.9)	1.021 (-0.3)	1.184 (-0.7)	1.235 (-1.2)	0.908 (-2.9)	
14	0.939	1.133	0.941	1.187	1.269	0.936		
	0.993 (5.8)	1.170 (3.3)	0.982 (4.4)	1.200 (1.1)	1.272 (0.2)	0.936 (-3.4)		
	0.989 (5.3)	1.162 (2.6)	0.976 (3.7)	1.188 (0.1)	1.264 (-0.4)	0.908 (-2.9)		
15	1.004	1.065	0.939	0.779				
	1.097 (9.2)	1.147 (7.7)	1.020 (8.6)	0.817 (4.9)				
	1.094 (8.9)	1.142 (7.2)	1.010 (7.5)	0.808 (3.7)				
CASMO-4E PARCS (%) KANT (%)								

Fig. 24. Radial power density distribution for BEAVRS Cycle 1.

The evaluated critical boron concentration at ARO (all rods out) HZP condition using Serpent2/KANT two-step procedure is shown in Table 10, where discrepancy with respect to the measured data is below 5 ppm. Further analysis including the measurement of control rod worth will be presented in a separate manuscript.

Figs. 23 and 24 exhibit radial thermal flux and power density distributions, where the former is directly compared with the measured detector signal data in the reference document [30]. For

radial power density distribution, the reference result was taken from CASMO-4E [36], and a direct comparison with other two-step analysis result, which has been obtained using SCALE/PARCS simulation, is also presented [6]. It can be seen that the KANT calculation result well resemble the reference, where deviation (in percent) is in the similar range with respect to the published PARCS calculation result.

As shown in Fig. 22, the actual power history for BEAVRS Cycle1

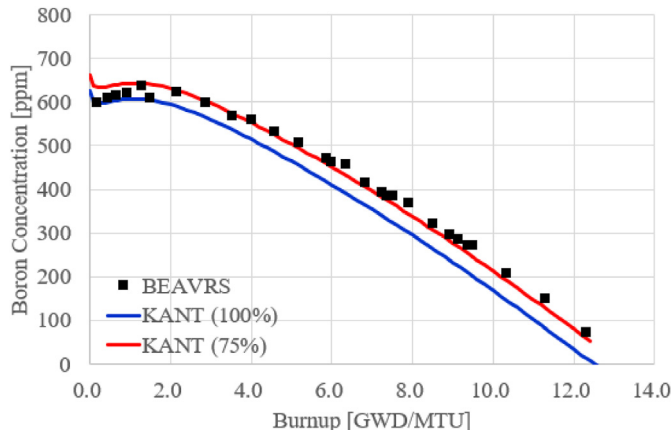


Fig. 25. Calculated CBC letdown curve using KANT.

operation is rather complicated. To circumvent such an issue, several reported works have employed a constant power level of either 75% or 100% of the nominal HFP condition for depletion calculation [5–7,37,38]. It must be noted that the average power level for the first cycle is about 75%, and such a power level must be used during depletion calculation for proper evaluation of Xenon-135 and Samarium-149 densities. Usage of a 100% power level not only intensifies the extent of negative feedback but also increases the saturated Xenon-135 concentration, leading to an underestimation of cycle length [37,38]. Fig. 25 depicts the critical boron concentration (CBC) letdown curve obtained from KANT two-step analysis, where a constant power level of 75% and 100% have been imposed. It could be seen that only the calculated CBC curve from a 75% power level well matches the reference values, whereas the CBC curve from a 100% power level tends to underestimate as discussed. Comprehensively, the present result attests to the applicability of KANT for multi-physics analysis regarding large-sized PWRs.

4. Conclusions

The KAIST Advanced Nuclear Tachygraphy (KANT) was recently developed and its accuracy for steady-state, transient, and macroscopic depletion with pin power reconstruction calculation has been tested using various benchmarks. The neutronics solver for KANT is based on the standard nodal expansion method (NEM) accelerated with various coarse-mesh finite difference (CMFD) methods, where discontinuity factors can be included for an accurate two-step analysis. To invoke feedback phenomenon stemming from the thermal-hydraulics effect, simplified axial balance equations and radial heat transfer equations are solved. Note that every transient calculation is treated with the implicit-Euler scheme in KANT.

The macroscopic depletion calculation is performed under the predictor-corrector scheme, and yield values associated with the simplified decay chains for Xenon-135 and Samarium-149 are adjusted for the preservation of proper number densities. The pin power reconstruction can be performed using either the conventional form function (FF) based approach or the embedded pin power reconstruction (EPPR) method in KANT, although only the result pertaining to the former approach is included in the manuscript.

The KANT simulation result for steady-state (IAEA 3-D and 4-group KOEBERG) and transient (LMW-LWR) sole neutronics benchmark, i.e., no feedback effect, exhibited a marginal difference with respect to the reference. In addition, capacity for mitigating

rod cuspding issue was also verified, where KANT supports both FWC and NSI methods. For the NEACRP 3-D PWR problem, which includes the TH feedback effect, generally good agreement was observed for HFP-related scenarios. Although some noticeable differences can be seen for HZP-based simulations, the extent of such deviation is definitely within the range of tolerance compared to other reported works.

For validation of macroscopic depletion capability alongside pin power reconstruction, a small PWR problem based on KAIST benchmark has been solved. Both the multiplication factor and assembly-wise power density well resemble that of the reference whole core transport calculation implying accurate application of nodal balance via discontinuity factors. Through yield correction in the simplified decay chain models for Xenon-135 and Samarium-149, and inclusion of dependency with respect to power density, the macroscopic depletion well matched with the reference calculation result.

To verify the applicability of KANT for performing multi-physics analysis concerning large-sized PWRs, the BEAVRS Cycle1 benchmark has been solved. Descriptions for conducting lattice calculation, which includes branching conditions for the assessment of derivative terms, are presented. For HZP calculation, both the critical boron concentration and radial thermal flux/power profiles well resembled the reference result. The calculation of the boron letdown curve for HFP simulation under a 75% constant power level, which accommodates the complex power history of the BEAVRS Cycle 1, exhibited reasonable agreement with the reported CBC values.

Comprehensively, the demonstrated work in this manuscript enough validates the capability of KANT for being used as a multi-physics nodal code. Further validation of KANT regarding improved pin power reconstruction through EPPR method is planned for the near future. Such assessments comprehensibly will verify the general applicability of KANT for designing a reactor. In addition, the transient multi-physics computing efficiency of KANT will be improved through implementation of a quasi-static method [14] alongside adaptive time-step scheme.

Declaration of competing interest

The authors declare that they have no known competing financial interests or personal relationships that could have appeared to influence the work reported in this paper.

Acknowledgements

This work was supported by the National Research Foundation of Korea (NRF) Grants funded by the Korean government NRF-2016R1A5A1013919 and NRF-2021M2D2A2076383.

References

- [1] SSP-09/442-U, CASMO-4E: Extended Capability CASMO-4 User's Manual, Studsvik Scandpower, 2009.
- [2] SSP-09/447-U, SIMULATE-3: advanced three-dimensional two-group reactor analysis code user's manual, Studsvik Scandpower, 2009.
- [3] T. Downar, Y. Xu, V. Seker, PARCS NRC Core Neutronics Simulator Theory Manual, 2009 (Ann Arbor, MI).
- [4] J.Y. Cho, DeCART2D V1.1 User's Manual. KAERI/UM-40/2016, Korea Atomic Energy Research Institute, 2016.
- [5] Jin Young Cho, Jae Seung Song, Kyung Hoon Lee, Three Dimensional Nuclear Analysis System DeCART/CHORUS/MASTER, ANS Annual Meeting, Atlanta, 2013, June 16–20.
- [6] Piotr Darnowski, Michał Pawluczyk, Analysis of the BEAVRS PWR benchmark using SCALE and PARCS, NUKLEONIKA 64 (3) (2019) 87–96.
- [7] Jaakko Leppänen, Riku Mattila, Validation of the Serpent-ARES code sequence using the MIT BEAVRS benchmark – HFP conditions and fuel cycle 1 simulations, Annals of Nuclear Energy 96 (2016) 324–331.
- [8] K.S. Smith, Assembly homogenization techniques for light water reactor

- analysis, *Progress in Nuclear Energy* 17 (3) (1986) 303–335.
- [9] Jaeha Kim, Yonghee Kim, Three-dimensional pin-resolved transient diffusion analysis of PWR core by the Hybrid coarse-mesh finite difference algorithm, *Nuclear Science and Engineering* 194 (2020) 1–13.
- [10] K.R. Rempe, K.S. Smith, A.F. Henry, SIMULATE-3 pin power reconstruction: methodology and benchmarking, *Nuclear Science and Engineering* 103 (1989) 334.
- [11] H. Finnemann, F. Bennewitz, M.R. Wagner, Interface current techniques for multidimensional reactor calculations, *Atomkernenergie* 30 (1977) 123–128.
- [12] R.D. Lawrence, Progress in nodal methods for the solution of the neutron diffusion and transport equations, *Progress in Nuclear Energy* 17 (3) (1986) 271–301.
- [13] Seongdong Jang, Yonghee Kim, Improved macroscopic depletion in 2-D nodal analysis by 2x2 albedo-corrected parametrized equivalence constants method, *Annals of Nuclear Energy* 175 (2022), 109209.
- [14] Tae-suk Oh, Yonghee Kim, Polynomial relaxation in the quasi-static approach and its implementation in nonlinear reactor transient analyses, *Annals of Nuclear Energy* 158 (2021), 108271.
- [15] Tae-suk Oh, Yonghee Kim, Investigation of nodal numerical adjoints from CMFD-based acceleration methods, *Front. Energy Res.* 10 (2022), 873731.
- [16] D. Basile, M. Beghi, R. Chierici, E. Salina, E. Brega, COBRA-EN: an upgraded version of the COBRA-3C/MIT code for thermal hydraulic transient analysis of light water reactor fuel assemblies and cores, *Radiat. Saf. Inf. Comput. Center, Oak Ridge Natl. Lab.* (1999).
- [17] C.W. Stewart, et al., VIPRE-01: a Thermal-Hydraulic Analysis Code for Reactor Cores. EPRI NP-2511 CCM, Electric Power Research Institute Research Project, 1983, 1584-1.
- [18] J.C. Gehin, A Quasi Static Polynomial Nodal Method for Nuclear Reactor Analysis, Ph. D. Thesis, Department of Nuclear Engineering, MIT, Cambridge, MA, USA, 1992.
- [19] Bumhee Cho, Nam Jin Cho, A nonoverlapping local/global iterative method with 2-D/1-D fusion transport kernel and p-CMFD wrapper for transient reactor analysis, *Annals of Nuclear Energy* 85 (2015) 937–957.
- [20] Maria Pusa, Jaakko Lepänen, Computing the matrix exponential in burnup calculations, *Nuclear Science and Engineering* 164 (2) (2010) 140–150.
- [21] Taesuk Oh, Yonghee Kim, Fission Yield Correction for Simplified Xe-135 and Sm-149 Decay Chains, *Transactions of the Korean Nuclear Society Spring Meeting*, Jeju, Korea, 2022, May 19–20.
- [22] Hwanyeal Yu, Seongdong Jang, Yonghee Kim, A new embedded analysis with pinwise discontinuity factors for pin power reconstruction, *Nuclear Science and Engineering* 195 (7) (2021) 766–777.
- [23] J. Leppanen, et al., The Serpent Monte Carlo code: status, development and applications in 2013, *Annals of Nuclear Energy* 82 (2015) 142–150.
- [24] Benchmark Problem Book, ANL-7416, Suppl. 2, Argonne National Laboratory, 1977.
- [25] E.Z. Muller, Z.J. Weiss, Benchmarking with the multigroup diffusion high-order response matrix method, *Annals of Nuclear Energy* 18 (9) (1991) 535–544.
- [26] Y.H. Kim, N.Z. Cho, A bilinear weighting method for the control rod cusping problem in nodal methods, *Journal of Korean Nuclear Society* 22 (1990) p238.
- [27] S. Langenbuch, et al., Coarse-mesh flux expansion method for the analysis of space-time effects in large light water reactor cores, *Nuclear Science and Engineering* 63 (1977) 437–456.
- [28] H. Finnemann, H. Bauer, A. Galati, NEACRP 3-D LWR Core Transient Benchmarks, vol. 93, NEA/NSC/DOC., 1993, 25[R]. [s.1.]: OECD/NEA.
- [29] N.Z. Cho, Benchmark Problems in Reactor and Particle Transport Physics: Benchmark Problem 1A ~ 3A, 2000.
- [30] D.N. Horelik, et al., Benchmark for evaluation and validation of reactor simulations, MIT Computational Reactor Physics Group 29 (August) (2018) rev09.
- [31] J. Kotchoubey, POLCA-T Neutron Kinetics Model Benchmarking, Master's Thesis, Division of Nuclear Reactor Technology, KTH Royal Institute of Technology, 2015.
- [32] K.S. Smith, An Analytic Nodal Method for Solving the Two-Group, Multidimensional Static and Transient Neutron Diffusion Equations, Master's Thesis, Department of Nuclear Engineering, MIT, Cambridge, MA, USA, 1979.
- [33] M.P. Knight, P. Bryce, Derivation of a refined PANTHER solution to the NEACRP PWR rod ejection transients, in: Proc. Joint Int. Conf. Mathematical Methods and Supercomputing for Nuclear Applications, Saratoga Springs, N.Y., American Nuclear Society, vol. 1, 1997, pp. 302–313.
- [34] H. Finnemann, H. Bauer, A. Galati, R. Martinelli, Results of LWR core transient benchmarks. https://inis.iaea.org/search/search.aspx?orig_q=RN:25052610, 1993.
- [35] <https://engineering.purdue.edu/PARCS/Code/TestSuite/Calculation/Mode/StandaloneMode/NEACRPPWR>.
- [36] C. Wan, L. Cao, H. Wu, W. Shen, Uncertainty analysis for the assembly and core simulation of BEAVRS at HZP conditions, *Nuclear Engineering and Design* 314 (2017) 11–19.
- [37] Min Ryu, et al., Solution of the BEAVRS benchmark using the nTRACER direct whole core calculation code, *Journal of Nuclear Science and Technology* 52 (7–8) (2015) 961–969.
- [38] Kan Wang, et al., Analysis of BEAVRS two-cycle benchmark using RMC based on full core detailed model, *Progress in Nuclear Energy* 98 (2017) 301–312.